

Experimental discovery of nodal chains

Qinghui Yan^{1,2}, Rongjuan Liu¹, Zhongbo Yan³, Boyuan Liu¹, Hongsheng Chen², Zhong Wang^{3,4} and Ling Lu^{1*}

Three-dimensional Weyl and Dirac nodal points¹ have attracted widespread interest across multiple disciplines and in many platforms but allow for few structural variations. In contrast, nodal lines^{2–4} can have numerous topological configurations in momentum space, forming nodal rings^{5–9}, nodal chains^{10–15}, nodal links^{16–20} and nodal knots^{21,22}. However, nodal lines are much less explored because of the lack of an ideal experimental realization^{23–25}. For example, in condensed-matter systems, nodal lines are often fragile to spin-orbit coupling, located away from the Fermi level, coexist with energy-degenerate trivial bands or have a degeneracy line that disperses strongly in energy. Here, overcoming all these difficulties, we theoretically predict and experimentally observe nodal chains in a metallic-mesh photonic crystal having frequency-isolated linear band-touching rings chained across the entire Brillouin zone. These nodal chains are protected by mirror symmetry and have a frequency variation of less than 1%. We use angle-resolved transmission measurements to probe the projected bulk dispersion and perform Fourier-transformed field scans to map out the dispersion of the drumhead surface state. Our results establish an ideal nodal-line material for further study of topological line degeneracies with non-trivial connectivity and consequent wave dynamics that are richer than those in Weyl and Dirac materials.

A nodal line is the extrusion of a Dirac cone, arguably the most intriguing two-dimensional band structure, into three-dimensional momentum space. They share the same local Hamiltonian $H(\mathbf{k}) = k_x\sigma_x + k_y\sigma_y$ that can be protected by the \mathcal{PT} symmetry forbidding the mass term of σ_z in the whole Brillouin zone, where \mathcal{P} is parity inversion and \mathcal{T} is time-reversal symmetry. A single nodal line forms a closed ring, due to the periodicity of the Brillouin zone, and the Berry phase around the node is π . Surprisingly, it was recently proposed¹¹ that nodal rings can be chained together as shown in Fig. 1a. The Berry phase around the chain point, enclosing two nodal lines, is 0 ($=\pi + \pi$). We show, in Fig. 1b, that the local chain Hamiltonian can be written as $H(\mathbf{k}) = k_x\sigma_x + (k_yk_z + m_z)\sigma_z$, when the mass term $m_z = 0$. The vanishing mass $m_z = 0$ can be guaranteed by an extra symmetry other than \mathcal{PT} . One example is the mirror (or glide) symmetry $M_z = \sigma_x$ that flips z coordinates, shown in Fig. 1b as a yellow plane. In the presence of the mirror, the two nodal lines cross at the origin. The red nodal line locates at the intersection between the planes of $k_x = 0$ and $k_y = 0$ and the blue nodal line locates at the intersection between the planes of $k_x = 0$ and $k_z = 0$. When the mirror symmetry is broken ($m_z \neq 0$), the chain point is lifted and the nodal lines become hyperbolic.

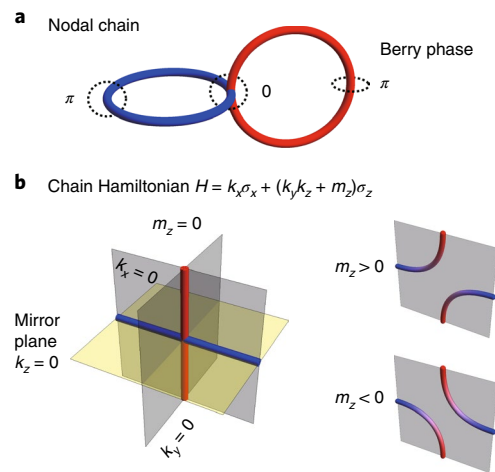


Fig. 1 | Nodal-chain Hamiltonian and stability. **a**, Illustration of the simplest chain structure between two rings. The Berry phase around the chain point is 0, in contrast to the π Berry phase of nodal lines. **b**, The chain point is the crossing between two nodal lines defined between three zero planes. The third plane in yellow represents the mirror plane protecting the chain point. When the mirror symmetry is broken by the mass term m_z , the chain point splits.

We designed a metallic-mesh three-dimensional photonic crystal with frequency-isolated nodal chains. The structure is shown in Fig. 2a. The yellow box denotes the cubic unit cell of space group $Pm\bar{3}m$, no. 221. Intersecting at the centre of the unit cell are three square rods along x , y and z directions, respectively. Numerically, we treat the metallic surfaces as perfect electric conductors, which is a good approximation for metals at microwave frequencies. We note that similar metallic-mesh structure has also been used for low-frequency plasmons²⁶, particle accelerators²⁷, novel metamaterials²⁸ and invisible medium²⁹.

Shown in Fig. 2b, the third and the fourth bands cross linearly, forming line degeneracies of nodal chains. The chain structure is plotted in Fig. 2c, where all nodal lines are chained across the entire Brillouin zone. There are three red rings centred at the X points on each face and three blue rings centred at the M points on each hinge. The same colored rings are related by the C_3 rotation symmetry along $\langle 111 \rangle$ directions. Each blue ring is chained with the neighbouring red rings perpendicular to it. All chain points lie in and are protected by the $\{001\}$ mirror planes. The band-structure evolution of metallic meshes of various filling ratios are presented in the Supplementary Information.

¹Institute of Physics, Chinese Academy of Sciences/Beijing National Laboratory for Condensed Matter Physics, Beijing, China. ²College of Information Science and Electronic Engineering, State Key Laboratory of Modern Optical Instrumentation, Zhejiang University, Hangzhou, China. ³Institute for Advanced Study, Tsinghua University, Beijing, China. ⁴Collaborative Innovation Center of Quantum Matter, Beijing, China. Qinghui Yan and Rongjuan Liu contributed equally to this work. *e-mail: linglu@iphy.ac.cn

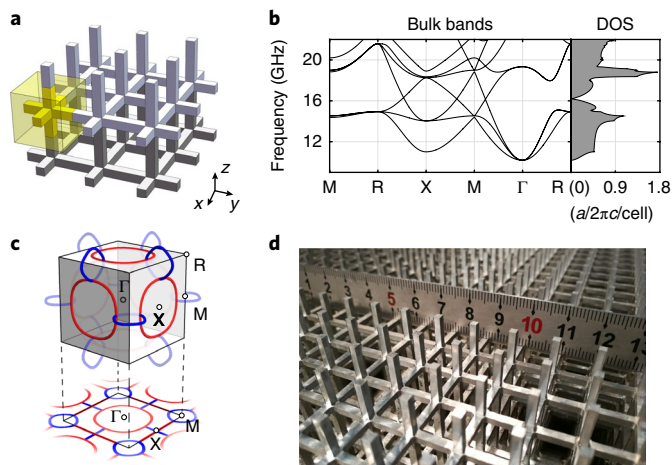


Fig. 2 | Nodal-chain photonic crystal. **a**, An illustration of the metallic-mesh three-dimensional photonic crystal. The yellow cube denotes a symmetric simple-cubic unit cell. **b**, The bulk band structure and DOS. The nodal-chain frequency is about 16.2 GHz. **c**, The structure of nodal chains in the Brillouin zone. The three blue rings are chained with the three red rings. **d**, The top surface of the sample made of aluminium alloy. The bottom surface is a flat mesh. The lattice constant is 11.6 mm and the rod width is 2 mm.

An important feature of this nodal chain is the low dispersion of the degeneracy frequencies, which is below 1% for the variation ($\Delta\omega/\omega_{\text{middle}}$) in the entire Brillouin zone. This is supported by the density of states (DOS) calculations³⁰ on the right of Fig. 2b. There is a clear dip in the DOS increasing linearly away from the nodal-chain frequency.

In experiment, we adopted aluminium as the material of choice for its high conductivity, low weight and low cost. The fabricated sample is shown in Fig. 2a with a lattice constant of

11.6 mm and a rod width of 2 mm. The resulting nodal-chain frequencies are very close to 16.2 GHz, as shown in Fig. 2b. The sample is stacked with nine identical layers and each layer has 30×30 unit cells. Every layer was milled and drilled from a plain aluminum plate. For assembling, handling and alignment, we reserved frames around each layer. The final size for one layer is $37 \text{ cm} \times 37 \text{ cm} \times 10.44 \text{ cm}$.

We carried out angle-resolved transmission to measure the nodal-chain bulk states. As shown in Fig. 3a, we used a similar set-up as in ref.⁵ to detect the frequency-resolved transmission as a function of the incident angle. As a result, angle-resolved transmission measures the bulk states projected along the normal direction (z) of the incident surface of the sample. In the in-plane directions on the surface, momenta are conserved. Figure 3b shows the [001] projection of nodal chains from numerical calculations, illustrated in Fig. 2c. A vector network analyser was used to collect data. A pair of prisms, with refractive index of 4, were used to increase the incident momenta and probe more areas in the reciprocal space (not shown in Fig. 3a). For comparison, we present the results without the prisms in Supplementary Information.

The comparisons between experimental results and projected band structures are shown in Fig. 3c–f for four different angles of $\theta = 0, 15, 30$ and 45° . With over 25 dB attenuation in bandgaps, results are clear and in good agreement with theory. The transmission data for separate polarization channels are presented in the Supplementary Information.

We performed Fourier-transformed field scans to measure the surface states of our nodal-chain sample. A nodal-line material is known to support a drumhead surface state, which is a sheet of surface dispersion enclosed by the projected nodal-line bulk states in the surface Brillouin zone. We form a surface by placing an aluminum plate 1 mm above the sample (001) surface, in order to isolate the free-space photon modes while leaving space for the near-field scanning probes. The set-up is shown in Fig. 4a and the surface band structure is plotted in Fig. 4b. The surface state is highlighted in red.

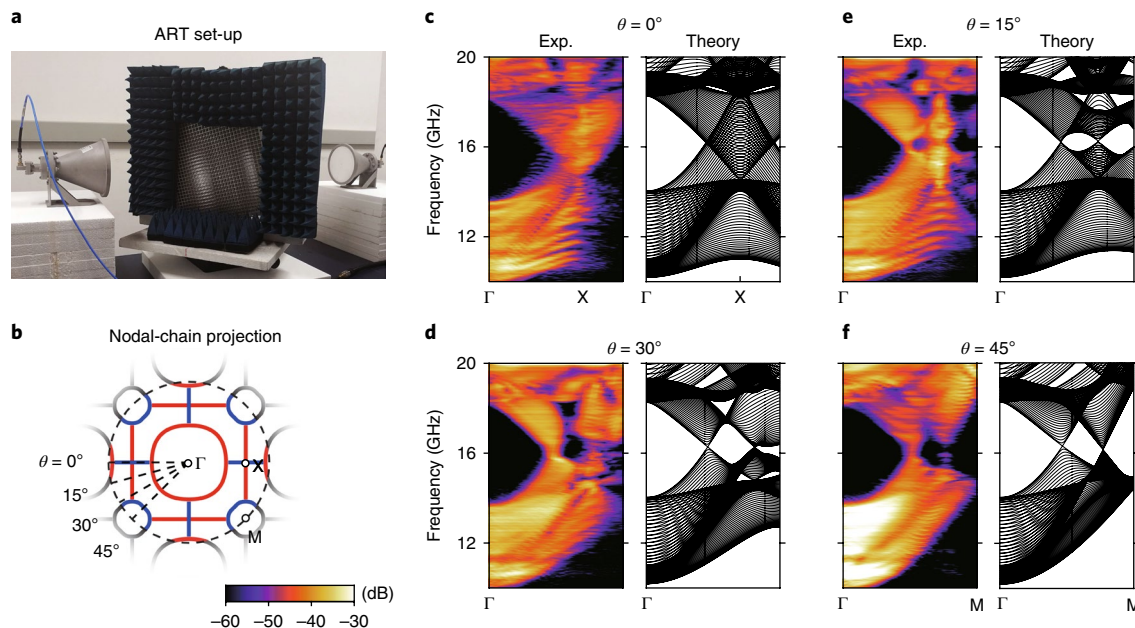


Fig. 3 | Angle-resolved transmission (ART) measurement of nodal-chain bulk states. **a**, The experimental set-up. **b**, Projective view of nodal chain in [001] direction. The dashed circle is the light cone in the prism at 16.2 GHz, which is the maximum momentum of the incident photon on the sample after the prism. Four dashed radii denote the four scan directions. **c–f**, Bulk experimental data compared with theoretical calculations for different θ values. The agreement is excellent.

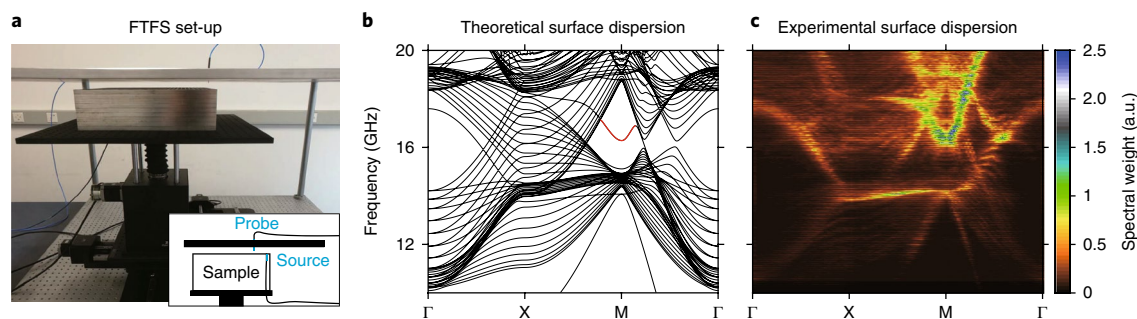


Fig. 4 | Fourier-transformed field (FTFS) scan measurement of the drumhead surface state. We measured the bottom surface of a flat mesh. **a**, Photograph and schematic illustration of the two-dimensional profiler. **b**, Theoretical calculation of the surface band structure. The supercell consists of 11 unit cells, with a 1 mm air gap to the upper perfect electrical conductor boundary. Plotted in red is the drumhead surface dispersion. **c**, The experimental Fourier-transformed field scans plotted in a linear scale. The surface modes appear at about 17 GHz, which matches the theoretical prediction. Other surface dispersions and some bulk bands can also be seen with lower intensities.

During the field scan, a broadband source was fixed inside the sample to excite both the surface and the bulk states. The probe was placed inside the hole in the centre of the aluminum board. The details of the profiler are presented in the Supplementary Information. During the measurement, the sample moved in plane on the guiding rails and the probe scanned across the sample surface point by point. Both the amplitude and the phase of the local fields were recorded at each frequency by the network analyser.

We then Fourier-transformed the field data from real space to reciprocal space and summed up the amplitudes in all equivalent Bloch momenta to the first Brillouin zone. Details of data processing are in the Supplementary Information. In Fig. 4c, the resulting intensity map is directly compared with the dispersion calculations. The drumhead surface modes at about 17 GHz are consistently seen in both theory and experimental data. A doubly degenerate drumhead due to the C_{4v} symmetry, of a different surface termination, is plotted in the Supplementary Information.

Our finding may inspire searches for ideal nodal lines in other material platforms, and stimulate experimental realizations of non-trivial nodal-line structures, such as nodal links¹⁷ and nodal knots²².

Data availability. The data that support the plots within this paper and other findings of this study are available from the corresponding author upon reasonable request.

Received: 21 June 2017; Accepted: 18 December 2017;
Published online: 19 February 2018

References

- Armitage, N. P., Mele, E. J. & Vishwanath, A. Weyl and Dirac semimetals in three dimensional solids. Preprint at <https://arxiv.org/abs/1705.01111> (2017).
- Burkov, A. A., Hook, M. D. & Balents, L. Topological nodal semimetals. *Phys. Rev. B* **84**, 235126 (2011).
- Lu, L., Fu, L., Joannopoulos, J. D. & Soljacic, M. Weyl points and line nodes in gyroid photonic crystals. *Nat. Photon.* **7**, 294–299 (2013).
- Fang, C., Weng, H., Dai, X. & Fang, Z. Topological nodal line semimetals. *Chin. Phys. B* **25**, 117106 (2016).
- Lu, L. et al. Experimental observation of Weyl points. *Science* **349**, 622–624 (2015).
- Kim, Y., Wieder, B. J., Kane, C. L. & Rappe, A. M. Dirac line nodes in inversion-symmetric crystals. *Phys. Rev. Lett.* **115**, 036806 (2015).
- Yu, R., Weng, H., Fang, Z., Dai, X. & Hu, X. Topological node-line semimetal and Dirac semimetal state in antiperovskite Cu_3PdN . *Phys. Rev. Lett.* **115**, 036807 (2015).
- Fang, C., Chen, Y., Kee, H.-Y. & Fu, L. Topological nodal line semimetals with and without spin-orbital coupling. *Phys. Rev. B* **92**, 081201 (2015).
- Kobayashi, S. et al. Crossing-line-node semimetals: general theory and application to rare-earth trihydrides. *Phys. Rev. B* **95**, 245208 (2017).
- Weng, H. et al. Topological node-line semimetal in three-dimensional grapheme networks. *Phys. Rev. B* **92**, 045108 (2015).
- Bzdusek, T., Wu, Q., Riegg, A., Sigrist, M. & Soluyanov, A. A. Nodal-chain metals. *Nature* **538**, 75–78 (2016).
- Kawakami, T. & Hu, X. Symmetry-guaranteed and accidental nodal-line semimetals in fcc lattice. Preprint at <https://arxiv.org/abs/1611.07342> (2016).
- Yu, R., Wu, Q., Fang, Z. & Weng, H. From nodal chain semimetal to Weyl semimetal in HfC. *Phys. Rev. Lett.* **119**, 036401 (2017).
- Wang, S.-S., Liu, Y., Yu, Z.-M., Sheng, X.-L. & Yang, S. A. Hourglass Dirac chain metal in rhenium dioxide. Preprint at <https://arxiv.org/abs/1705.01424> (2017).
- Feng, X., Yue, C., Song, Z., Wu, Q. & Wen, B. Topological Dirac nodal-fermions in AlB_2 -type TiB_2 and ZrB_2 . Preprint at <https://arxiv.org/abs/1705.00511> (2017).
- Chen, W., Lu, H.-Z. & Hou, J.-M. Topological semimetals with a double-helix nodal link. *Phys. Rev. B* **96**, 041102 (2017).
- Yan, Z. et al. Nodal-link semimetals. *Phys. Rev. B* **96**, 041103 (2017).
- Chang, P.-Y. & Yee, C.-H. Weyl-link semimetals. *Phys. Rev. B* **96**, 081114 (2017).
- Zhong, C. et al. Three-dimensional pentagon carbon with a genesis of emergent fermions. *Nat. Commun.* **8**, 15641 (2017).
- Chang, G. et al. Topological Hopf and chain link semimetal states and their application to Co_2MnGa . *Phys. Rev. Lett.* **119**, 156401 (2017).
- Ezawa, M. Topological semimetals carrying arbitrary Hopf numbers: Fermi surface topologies of a Hopf link, Solomon's knot, trefoil knot, and other linked nodal varieties. *Phys. Rev. B* **96**, 041202 (2017).
- Bi, R., Yan, Z., Lu, L. & Wang, Z. Nodal-knot semimetals. *Phys. Rev. B* **96**, 201305 (2017).
- Bian, G. et al. Topological nodal-line fermions in spin-orbit metal PbTaSe_3 . *Nat. Commun.* **7**, 10556 (2016).
- Schoop, L. M. et al. Dirac cone protected by non-symmorphic symmetry and three-dimensional Dirac line node in Zr-SiS . *Nat. Commun.* **7**, 11696 (2016).
- Chen, C. et al. Dirac line nodes and effect of spin-orbit coupling in the nonsymmorphic critical semimetals MSi ($M = \text{Hf, Zr}$). *Phys. Rev. B* **95**, 125126 (2017).
- Pendry, J. B., Holden, A. J., Stewart, W. J. & Youngs, I. Extremely low frequency plasmons in metallic mesostructures. *Phys. Rev. Lett.* **76**, 4773 (1996).
- Shapiro, M. A., Sirigiri, J. R., Temkin, R. J. & Shvets, G. 3D metallic lattices for accelerator applications. In *Proceedings of the Particle Accelerator Conference, 2005. PAC 2005* 1838–1840 (IEEE, 2005).
- Chen, W.-J. & Chan, C. T. Metamaterials with index ellipsoids at arbitrary k-points. Preprint at <https://arxiv.org/abs/1611.08099> (2016).
- Ye, D., Lu, L., Joannopoulos, J. D., Soljacic, M. & Ran, L. Invisible metallic mesh. *Proc. Natl Acad. Sci. USA* **113**, 2568–2572 (2016).
- Liu, B., Johnson, S. G., Joannopoulos, J. D. & Lu, L. Generalized Gilat-Raubenheimer method for density-of-states calculation in photonic crystals. Preprint at <https://arxiv.org/abs/1711.07993> (2017).

Acknowledgements

We thank Yang He, Chen Fang and Hongming Weng for discussions. The authors were supported by the National Key R&D Program of China under Grant Nos 2017YFA0303800 and 2016YFA0302400 and by NSFC under Project Nos 11721404 (L.L.), 11674189 (Z.Y., Z.W.), 61625502 (H.C.), 61574127 (H.C.), the Top-Notch Young Talents Program (H.C.) and the National Thousand Young Talents Program (L.L.) of China.

Author contributions

L.L. proposed and led the project. R.L. fabricated the sample. Q.Y. and R.L. made the measurements. Q.Y. processed the data and carried out the calculations. Z.W. and Z.Y. came up with the k,p model and enhanced the theoretical understanding. All authors contributed to the discussion and writing of the manuscript.

Competing interests

The authors declare no competing financial interests.

Additional information

Supplementary information is available for this paper at <https://doi.org/10.1038/s41567-017-0041-4>.

Reprints and permissions information is available at www.nature.com/reprints.

Correspondence and requests for materials should be addressed to L.L.

Publisher's note: Springer Nature remains neutral with regard to jurisdictional claims in published maps and institutional affiliations.